用√符号选择一类	
教　学	
科　研	√
编号（由专家组填写）	

第十一届全国高校物理实验教学研讨会
本科学生物理实验论文评比表

学生姓名：郭曜榛

申报学校：同济大学

联系方式：电话：17717055926

QQ：554322943

E-mail：1753921@tongji.edu.cn

填表日期：2021 年 6 月 22 日

全国高校物理实验教学研讨会组委会制

二〇二〇年一月

学生作者及发表有关物理实验论文情况

姓名	郭曜榛	性别	男	出生年月	1999.8.22
学校名称	同济大学				
入学时间	2017.9	毕业时间	2022.6		
学 号	1753921				

参评论文：（题目. 杂志名称，卷/期、页、年）

Enhancement and directional control of light output of scintillators by using microlens arrays: A numerical simulation study. Nuclear Instruments and Methods in Physics Research Section A Accelerators Spectro meters Detectors and Associated Equipment,2020, Vol.974:164206

（注：论文的第一作者必须为大学本科生，且其论文研究工作是在本科生阶段完成的，到现场答辩的为该论文的学生作者之一。）

论文作者情况（按发表论文作者顺序列出）：

姓名	身份	单位	作用/贡献
郭曜榛	本科生	同济大学	观点提出，模拟撰写，模拟计算
袁荻	博士生	同济大学	理论指导
李忠睿	本科生	同济大学	模拟计算
朱陈毓	本科生	同济大学	模拟计算
戴子轩	本科生	同济大学	数值计算
刘波*	教授、指导老师	同济大学	理论指导

简要介绍（研究背景、问题、方法、创新点、学术及应用价值和引用情况等）：

研究背景：

闪烁探测作为光学探测的一种必要手段，在高能物理实验、核物理实验和核医学成像领域都具有举足轻重的地位。但囿于闪烁体本身较高的折射率，限制了闪烁光子的出射，在一定程度上降低了光输出，降低了闪烁体的有效光产额。本项目拟采用自组装微透镜阵列为基础的人工微透镜阵列，探索对闪烁体光提取效率提高和发光方向性能有效控制的手段。以典型的薄膜和块体闪烁体为基本研究对象，结合闪烁探测的需求探讨其设计原则，根据其物理机制作针对性分析，建立能在最大程度上符合设计需求以及最贴近其物理机制的模型，利用软件仿真和实验验证的方式，最终得出结论，这对辐射探测应用有重大意义。不同于传统模式的注重闪烁体材料的有关凝聚态物理的光提取方法，本项目的创新点更注重于光学和电磁学原理,在物理机制的诠释上有重要的意义。

研究问题：

（1）研究闪烁体本身发光的原理

所使用的块状闪烁体 LYSO、BGO 具有折射率较高，形状特殊的特点，但正是因为其形状特殊，存在六个出射界面，导致每个出射界面引起的全反射导致出射效率低下，即大部分光线被“困”于闪烁体内部，这是我们拟解决和研究的首要问题。其次，闪烁体本身是受激发光，其本身可看作内部的一个或多个具有空间衰减特性的点光源发光，因而本项目将研究存在光强吸收情况下的多个或单个点光源的发光情况。

（2）研究利用人工微透镜阵列调控发射方向性的物理过程

尽管闪烁体所发出的光线是全角度范围，但实际上每个角度的强度权重各不相同，存在最大值点和最小值点。对于某些探测情况和领域，只有特定角度的光子可以被接收利用或只需要最大强度的特定角度光，所以需要此方向的光能够达到足够强度，并抑制其他方向的光。针对此背景，本项目拟通过控制表面微透镜阵列的方式探究被提取光的发光方向同结构参数的关系，探究调控方向性和强度的手段和方法。

研究方法：

(1)理论计算方法

针对光提取的方向性需求与强度要求，本项目拟建立合适的物理模型进行分析。对于周期性排列的人工微透镜，我们可以从个体进行物理机制分析，进而扩展到周期整体。因此，对于原理，将会使用到包括光学的部分定律和经典麦克斯韦方程组，以及在数学上有关积分和级数的方法对个体和整体进行剖析。这里我们拟采用经典光学的理想光线传播方式简化计算，后期根据对比实验和仿真结果的差异再对模型和方法进行修正，对计算结果进行补偿，最终得出较为合理的结果，从而对微透镜控制闪烁体发光的机制给出物理解释。

	(2)数值仿真方法 研究的出射光线时，由于涉及到光线追迹，需要考虑到光在闪烁体内部的传播情况，因而，一般的单光线、单点源的模拟软件很难适应该项目的需求。如果需要设计到电场与磁场分布的情况，软件需要能够在微分运算上具备强大的能力。此外，考虑到部分材料会有自吸收的情况，我们拟采用自由度较高的仿真软件，在其中加入有关自吸收的修正，使仿真结果相对合理。 **创新点：** （1）闪烁体研究方法的创新 本项目对于闪烁体的研究方法，将基于传统光学以及电磁学的基本原理而不是凝聚态物理和材料工程的方式，利用微透镜阵列本身的结构特性，实现对内全反射光的有效提取，增加闪烁体的有效光产额，也可以实现发射方向性的调控。作为一种全新的研究闪烁体的方法，其具有重要的创新意义。 （2）设计原则的创新 不同于传统的仅基于光提取的研究方法，本项目更注重于针对薄膜闪烁体和块体闪烁体光提取的方向性调控的物理模型和设计原则，能够同时解决涉及到光输出和方向调控的专业性问题，从而拓宽了对于闪烁体的模型限制，更适应于闪烁体应用的需求，对闪烁探测领域的发展具有重要的推进意义。 **学术及应用价值：** 近年来，通过自组装方法制备人工光子微结构的技术逐渐发展起来，其操作简便、价格便宜、易于制备的优点使其具有突出的优势。利用自组装的聚苯乙烯或二氧化硅微球可以组成单层六角密堆积结构的光子微结构，这种周期性排列的结构因为基于闪烁体表面，与闪烁体存在一个折射率梯度，在一定程度上会对闪烁体的出射光进行控制，包括其方向性与强度都会得到一定程度的改变。 和本项目类似的工作开展在国内外报道较少，西欧的核子中心所报道的采用电子束刻蚀制备毫米大小的二维平板光子晶体提高 LYSO 等闪烁体的提取效率。本项目采用较为创新的方法，使用全新的微透镜阵列模式对闪烁体表面进行改变，是在此基础上比较独特的方法。
指导教师评语	指导教师姓名：刘波　职称：教授 **对学生发表论文评语及论文情况说明：** 闪烁体通常具有较高的折射率从而限制了其光输出效率，该论文设计了基于微透镜阵列的表面结构，以提高闪烁体的光输出效率。论文采用数值模拟的方法开展研究，获得了微结构阵列增强光输出和光输出方向性调控的物理机理，获得了优化的参数结构。作者基于光线追踪的原理，自行编制了相关模拟程序，所得结果可信，物理分析合理，对于发展高效率闪烁探测器具有重要借鉴意义。 指导教师（签名）：刘波　2021年6月24日

学校推荐意见	本论文很好地将数值模拟与物理模型结合，对物理图像进行了详细的讨论与解释，体现了本科生的科研能力与探索精神，具有很高的创新意义。 负责人（签名）：　　　公章　　　年　月　日 同济大学物理科学与工程学院
大会学术组专家意见	专家组组长（签名）：　　　年　月　日
评比结果	理事长（签名）　　　年　月　日

Nuclear Inst. and Methods in Physics Research, A 974 (2020) 164206

Contents lists available at ScienceDirect

Nuclear Inst. and Methods in Physics Research, A

journal homepage: www.elsevier.com/locate/nima

Enhancement and directional control of light output of scintillators by using microlens arrays: A numerical simulation study

Yaozhen Guo, Di Yuan, Zhongrui Li, Chenyu Zhu, Zixuan Dai, Bo Liu *

Shanghai Key Laboratory of Special Artificial Microstructure Materials and Technology, School of Physics Science and Engineering, Tongji University, Shanghai 200092, PR China

ARTICLE INFO

Keywords:
Microlens array
Scintillator
Enhancement of light output
Control of directional emission

ABSTRACT

In this investigation, we have carried out the simulations of light output and the directionality of emission from scintillators coated with microlens arrays by using the ray-optics method. We systematically analyze the impact of an individual microlens at different positions on the light output intensity and the directional control, followed by an entire understanding of microlens arrays. It is found that microlens arrays can be used to increase the extraction efficiency and control the directionality of emission of scintillation light. The multiple reflections by the lateral and bottom surfaces play an important role. A comprehensive understanding of the impact of the ratio of width and thickness of a scintillator and the refractive index of microlens is presented and discussed in details. The maximum angle-integrated intensity could be obtained when the refractive index of microlens is slightly larger than that of scintillator. Simulations based on genetic algorithms can be used to efficiently design the parameters of microlens arrays with a specific target of a combination of emission angle and total emission intensity.

1. Introduction

Scintillators which can convert the energy of ionizing radiation into a number of photons in visible or near-visible range play an important role in the field of nuclear radiation detection, such as nuclear physics experiments, national security, nuclear medical imaging and dark matter detection [1–6].

In the practical applications, the light extraction efficiency of scintillators is limited by total internal reflection due to their high refractive indices, thus reducing the performance of detectors. In recent years, some schemes based on the microstructures such as photonic crystals [7–12], plasmonic lattices [13,14] have been proposed, which exhibit obvious benefits to the light extraction and directional emission control. However, the microstructures with sub-wavelength and wavelength scales usually exhibit significant wavelength-dependence due to the diffractive nature.

Microlens arrays (MLAs) with the individual microlens size of 10 to 100 μm could be used to control the light propagation based on geometrical optics, obtaining extensive applications in light emitting diodes, illumination, and collimating or focusing in imaging systems [15–18].

MLAs coated on the surface of scintillators can control the scintillation light output and control the directional emission. Such control process could be complicated since the propagation of light could be affected by the size and the interface of scintillators. In this paper, we have carried out the simulations based on the ray-optics method, providing a comprehensive understanding of the critical factors of individual microlenses and their arrays affecting on the light output of scintillators.

2. Methods of structure design and numerical simulations

Fig. 1(a) is the schematic illustration of a scintillator (refractive index of n_1) coated with a square-packed MLA (refractive index of n_2) on its surface. The individual microlenses are hemispheres with a diameter of D. As shown in Fig. 1(b), a far-field receiver in the simulations is used to collect the data of light intensity of each point P which can be defined by a zenith angle (φ_z), an azimuth angle (θ_A) and a distance between the center of the scintillator and the receiver (r).

The numerical simulations based on the ray-optics method traverse all the ray vectors and use vectors to trace light rays. This method has a higher precision but is more computational load compared with the traditional Monte Carlo method [19]. An isotropic scintillation light source is set at the center of the scintillator. The light rays from the source have their optical paths defined by three-dimensional vectors. At boundaries or interfaces, the direction and intensity of the transmitted and the reflected light rays are calculated by a transformational matrix. The intensity of each light ray emitted per unit time is defined as I_0. When its intensity becomes to be less than I_T which is set to be 3%

* Corresponding author.
E-mail address: lbo@tongji.edu.cn (B. Liu).

https://doi.org/10.1016/j.nima.2020.164206
Received 8 May 2020; Received in revised form 25 May 2020; Accepted 28 May 2020
Available online 30 May 2020

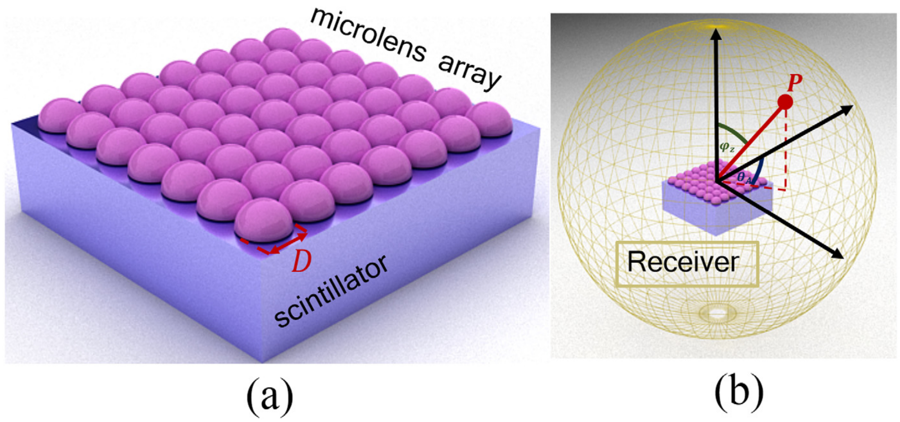

Fig. 1. (a) Schematic illustration of a scintillator coated with a microlens array on its surface. (b) Diagram of far-field detection.

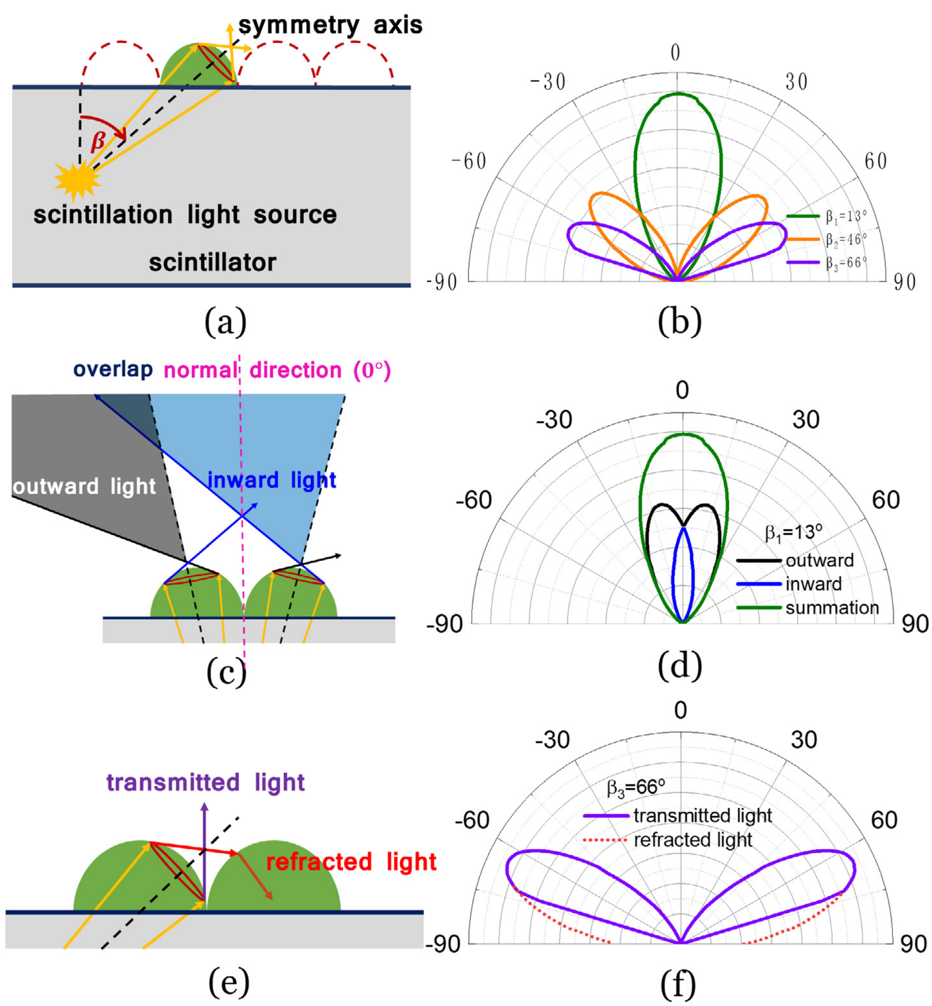

Fig. 2. (a) Definition of an individual microlens with its light ray paths. (b) Spatial distribution of light intensity for an individual microlens with representative angles of $\beta_1 = 13°$, $\beta_2 = 46°$ and $\beta_3 = 66°$. (c) Schematic illustration of light ray paths for the inward light and the outward light for the range of β_1. (d) Spatial distribution of light intensity of an individual microlens for $\beta_1 = 13°$, including the inward light, the outward light and their summation. (e) Schematic illustration of light ray paths for the transmitted light and the refracted light for the range of β_3. (f) Spatial distribution of light intensity of an individual microlens for $\beta_3 = 66°$, including the transmitted light and the refracted light.

of I_0, the calculation would be terminated. Finally, the data at each point P containing the information of the direction and intensity are recorded.

Genetic algorithms are used to obtain the optimal parameters [20]. A target parameter V is defined by the formula (1)

$$V = I_T(e^{\frac{I_{\theta_A}}{I_T}} - 1) \tag{1}$$

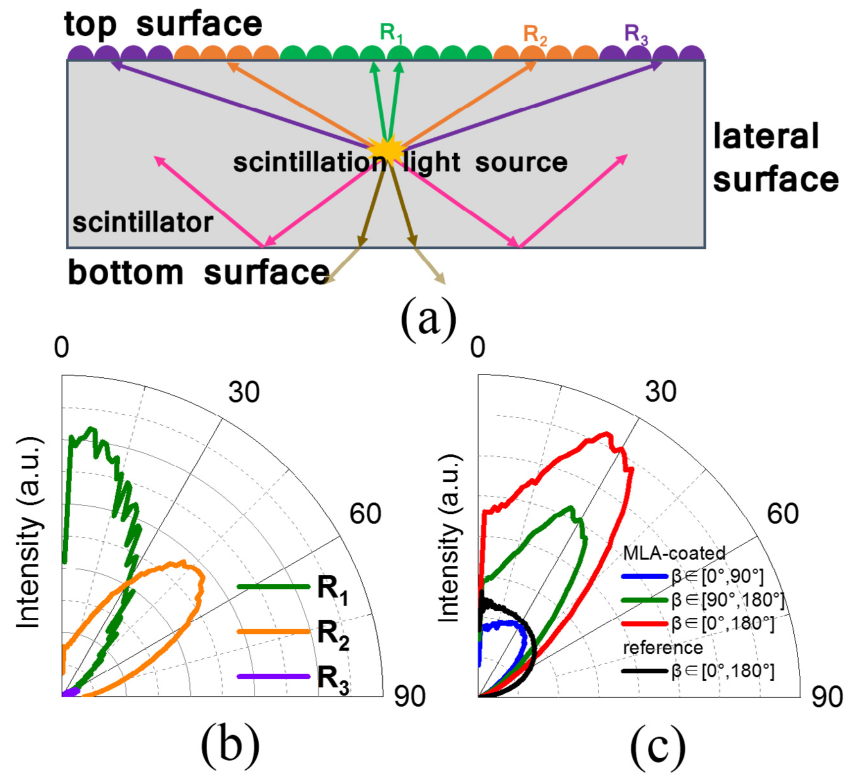

Fig. 3. (a) Schematic illustration of representative light ray paths for different regions. (b) Spatial distribution profiles of light intensity for the regions of R_1, R_2 and R_3. (c) Spatial distribution profiles of light intensity for the whole range of β including the downward emission.

where, I_T is the angle-integrated intensity, and $I_{\theta A}$ is the intensity at the azimuth angle of θ_A. When the parameter V reaches its maximum value, it means that not only a strong dependence on this angle is obtained, but also the overall light intensity is as strong as possible under such conditions. Therefore, V can characterize the angle-dependence of light output, concurrently taking into account the total intensity of light output.

3. Results and discussion

As an example, $Bi_4Ge_3O_{12}$crystals ($n_1 = 2.15$) are selected as the studied scintillators with the size of 18×18×3 cm^3. MLAs made of polystyrene ($n_2 = 1.59$) are coated on the surface of the scintillators. The diameter of an individual microlens is set to be $D = 10$ μm which is much larger than the emission wavelength of the $Bi_4Ge_3O_{12}$ scintillators so that the ray-optics is applicable. A crystal with the identical size is selected as a reference sample without MLAs.

For an isolated microlens, when light rays reach the boundary of the microlens, the spatial distribution of light intensity forms an escape cone which has a symmetry axis shown in Fig. 2(a). While for a MLA, the spatial distribution of light intensity will be affected by the surrounding microlenses. According to Appendix A, the magnitude of γ_{max} and β will determine the direction of symmetry axis. Therefore, it is necessary to divide the range of β into three regions of β_1, β_2, and β_3, which can be defined by the formula (2). In the range of β_1, an overlap appears, while in the range of β_3,the symmetry of distribution will be broken because of the surrounding microlenses.

$$\begin{cases} \beta_1 : 0 < \beta < 27.72°(\frac{1}{2}\gamma_{max}) \\ \beta_2 : 27.72° < \beta < 60°(90° - \arcsin\frac{1}{2}) \\ \beta_3 : \beta > 60° \end{cases} \quad (2)$$

The simulated spatial distribution of light intensity for an isolated microlens at three representative angles in each region is shown in Fig. 2(b), which indicates an obviously different spatial distribution in different β regions. In the range of β_1, the light rays close to the normal direction are defined as inward light rays, and the light rays far away from the normal direction are defined as outward light rays, as shown in Fig. 2(c). The simulated results shown in Fig. 2(d) suggest that the overlap region containing both of the inward and the outward light rays leads to the symmetry axis along the normal direction. In the range of β_2, the spatial distribution of light intensity exhibits a symmetrical pattern along the symmetry axis. While in the range of β_3, the transmitted light rays would be obscured and reflected into the crystal by the surrounding microlenses, as shown in Fig. 2(e). The simulated spatial distribution of light intensity for the transmitted light and the refracted light is shown in Fig. 2(f).

Due to the significantly different spatial distribution for the regions of β_1, β_2, and β_3, the top surface should be accordingly divided into three regions of R_1, R_2 and R_3, as shown in Fig. 3(a). Fig. 3(b) presents the spatial distribution profiles of light intensity for the regions of R_1, R_2 and R_3, which is an angle-integral intensity with their corresponding ranges of β_1, β_2, and β_3. For the sake of simplicity, we only plot the unilateral angle. Firstly, for the R_1 region, the maximum intensity appears at the angle of 0° with a rapid decrease for an increasing angle. Secondly, for the R_2 region, the spatial distribution of light intensity has a maximum intensity around the angle of 45°. Finally, the impact of the surrounding microlenses in the R_3 region will restrict severely the light extraction efficiency, making the R_3 region little contribution to the total light output.

In the above discussion, we only consider the upward emitted scintillation light for $\beta \in [0°, 90°]$. However, the downward emitted scintillation light rays for $\beta \in [90°, 180°]$ will be reflected by the lateral and bottom surfaces and thus have chances to reach the top surface. As a result, the reflected light rays could be extracted with the assistance of the lateral and bottom surfaces. It is therefore essential to consider the multiple reflections by the lateral and bottom surfaces. Fig. 3(c) displays the spatial distribution of light intensity, including the contributions from the upward light and the downward light. It is interesting

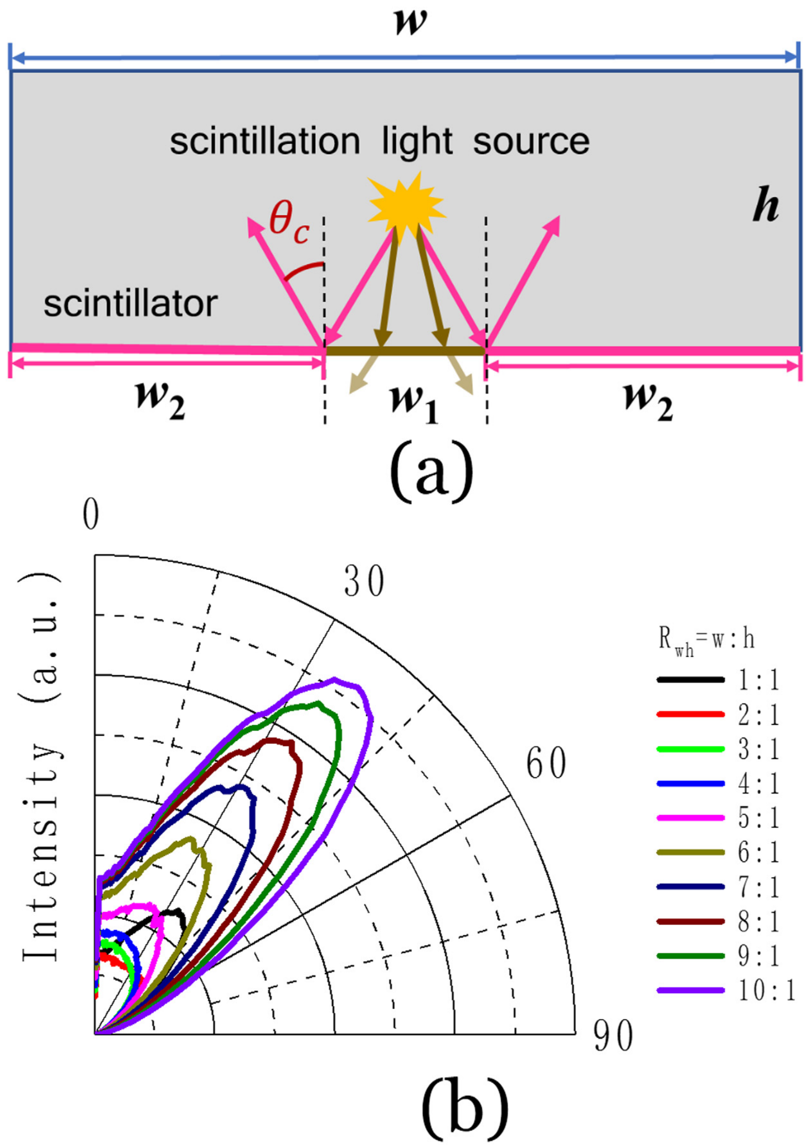

Fig. 4. (a) Schematic illustration of representative light ray paths while hitting the bottom surface. Here, θ_c is the critical angle, w is the width, h is the thickness, and w_1 (w_2) is the width corresponding to the region below (beyond) the critical angle. (b) Spatial distribution of light intensity for different values of R_{wh}.

to find that the contribution from the downward light is dominant. This consideration is analogy to an actual situation. Compared with the reference scintillator without MLAs, a 2.02-fold angle-integrated enhancement is obtained. Additionally, the directionality of emission controlled by MLAs exhibits a broad angular range, which is influenced by the thickness of scintillator due to the average effect.

The above results are obtained for the scintillator with a specific size. However, we have found that the multiple reflections by the lateral and bottom surfaces have a marked impact on the ultimate light output. It is thus expected that the ratio of width (w) and thickness (h) (labeled as $R_{wh} = w/h$) plays an important role. Fig. 4(a) presents the representative light ray paths while hitting the bottom surface. Here, θ_c is the critical angle, w is the width, h is the thickness, and w_1 (w_2) is the width corresponding to the region below (beyond) the critical angle. For $\beta < \theta_c$, most of the light rays will transmit through the bottom surface, and only a small fraction of light rays will encounter Fresnel reflection at the bottom surface. While for $\beta > \theta_c$, the light rays will be totally reflected by the bottom surface. If h is fixed, when w increases, w_1 remains unchanged, but w_2 also increases. As a result, when R_{wh} increases, the light extraction efficiency will be greatly improved due to the increased light rays reflected by the bottom surface. In addition, because a part of light rays are refracted into air through the bottom surface, the intensity around the normal direction reduces, thus making the maximum intensity concentrate on the range of angle from 30° to 45°.

The spatial distribution of light intensity for different values of R_{wh} is simulated with a fixed h value of 3 cm and variable w values. As shown in Fig. 4(b), it is found that for $R_{wh} = 1$, the light rays usually escape from the lateral surface but seldom reflect at the bottom surface, leading to the maximum intensity at 35°. When the values of R_{wh} increase to 2, 3 or 4, the lateral surface will reflect a part of light rays, leading to the maximum intensity at about 0°. However, when the values of R_{wh} continuously increase to 5 or larger, the intensity of reflected light rays by the lateral surface is much less than that by the bottom surface. As a consequence, the angle for maximum intensity will change to about 45°. Compared to the case of $R_{wh} = 1$, the angle-integrated enhancement ratio reaches 2.51 for the case of $R_{wh} = 10$.

In order to understand the impact of the refractive index of microlens n_2 on the extraction efficiency and the control of directional emission, the simulated results for different values of n_2 are presented in Fig. 5. The case for $n_2 = 1.0$ can be regarded as a reference case. As

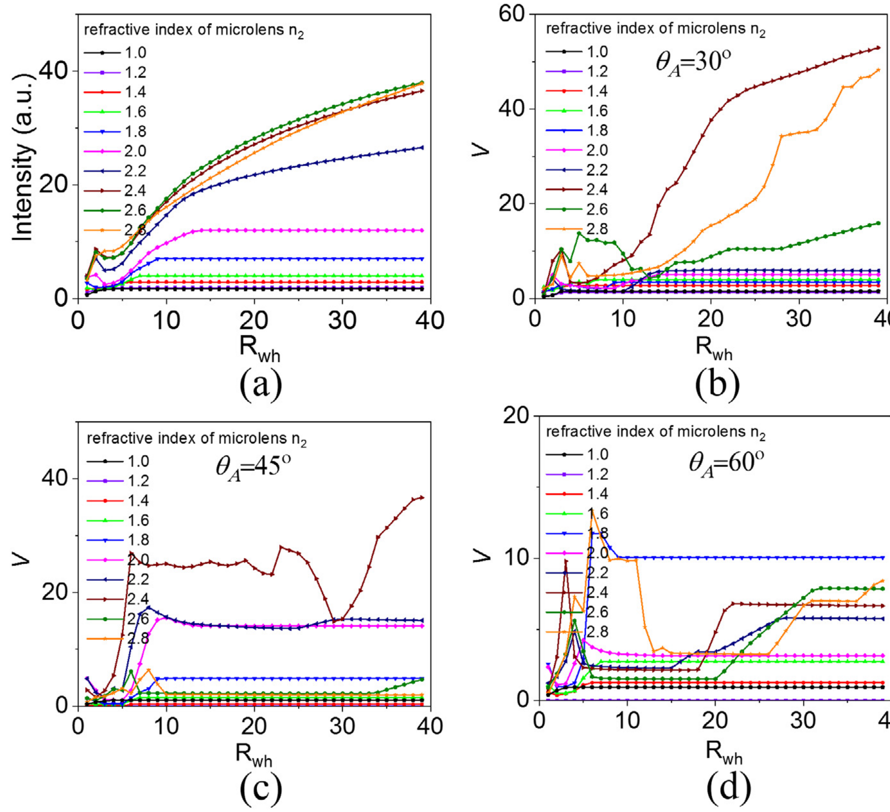

Fig. 5. (a) Angle-integrated intensity with a function of R_{wh} for different refractive indices of microlens n_2. (b), (c) and (d) V values with a function of R_{wh} for different refractive indices of microlens n_2 with the emission angles at 30°, 45° and 60°, respectively.

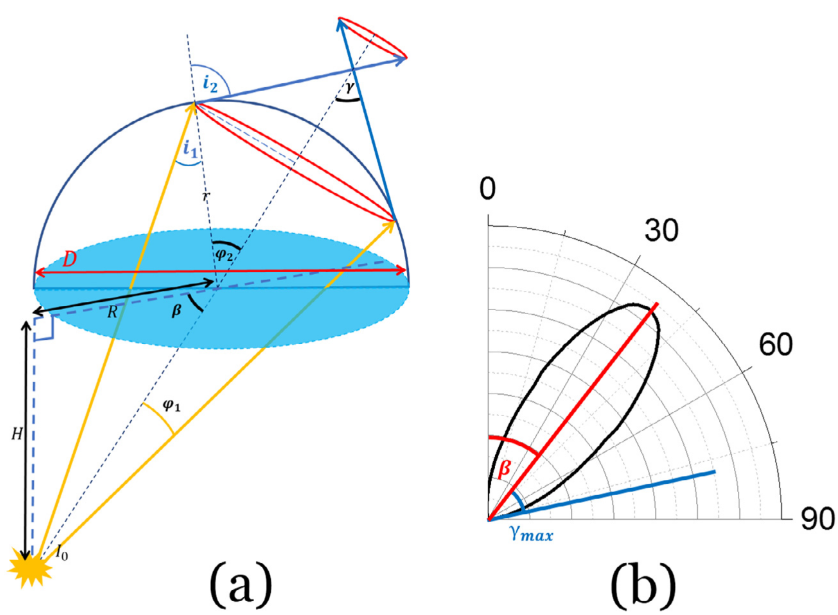

Fig. 6. (a) Definition of the related parameters in an individual microlens. (b) Spatial distribution of light intensity of an individual microlens.

shown in Fig. 5(a), when the values of n_2 are between 1.0 and 1.2, the angle-integrated intensity first increases and then stabilizes when $R_{wh} > 5$. When the values of n_2 is between 1.4 and 1.8, the angle-integrated intensity first decreases and then increases to a stable value when $R_{wh} > 9$. While, when the values of n_2 are larger than 2.0, the angle-integrated intensity exhibits a continuous increase with the increasing values of R_{wh}, except for a small dip at $R_{wh} = 5$. Large values of n_2 are beneficial to the enhancement of light extraction efficiency, especially for the cases with large values of R_{wh}. For example, one can find that when $R_{wh} = 2$, a 6.86-fold enhancement can be obtained with $n_2 = 2.4$, while when $R_{wh} = 39$, a 22.6-fold enhancement can be obtained with $n_2 = 2.6$. It is interesting to find that the maximum angle-integrated intensity could be obtained when the values of n_2 are slightly larger than those of scintillators. The main reason is that at this situation the scintillation light rays could easily enter the microlens. However, when the values of n_2 are much larger than those of scintillators, the light rays inside the

Table 1
Optimal parameters for the maximum values of V.

θ_A	n_2	R_{wh}	V_{max}
30°	2.44	38.06	48.26
45°	2.47	37.89	36.85
60°	1.86	9.08	11.73

microlens may be reflected at the interface of air, leading to reduction of light extraction efficiency.

Fig. 5(b), (c) and (d) show the simulated V values with a function of R_{wh} for different refractive indices of microlens n_2 with the emission angles at 30°, 45° and 60°, respectively. The results indicate that the values of n_2 can significantly control the directional emission, which is also strongly dependent on the values of R_{wh}. For the cases of θ_A = 30° and 45°, the highest values of V are obtained with n_2 = 2.4, which is mainly contributed from the high total intensity. When n_2 is larger than n_1, the directivity of emission is close to the normal direction. As shown in Fig. 5(d), for a large emission angle of 60°, the values of V become very small, compared with the cases of 30° and 45°. Moreover, it is also found that for large values of R_{wh}, the values of V decrease first and then increase, which could be due to the fact that the light rays focus on low angles for small values of R_{wh}, but distributed at high angles for large values of R_{wh}.

The optimal parameters for the maximum values of V shown in Table 1 are determined by genetic algorithms [21]. The optimal values of n_2 are 2.44, 2.47 and 1.86 for the target emission angles of 30°, 45° and 60°, respectively, which are basically consistent with the results in Fig. 5.

4. Conclusion

The present simulations demonstrate that MLAs can be used to increase the extraction efficiency and control the directional emission of scintillation light. Individual microlenses in different regions lead to different propagation behaviors of light rays. To understand the ultimate directional emission, the impact of lateral and bottom surfaces should be correctly considered, which implies that the multiple reflections by the lateral and bottom surfaces play important roles. The control of emission by MLAs is also strongly affected by the ratios of width and thickness of scintillators. It is found that the maximum angle-integrated intensity could be obtained when the refractive indices of microlenses are slightly larger than those of scintillators. The optimal parameters for the MLAs can be obtained by using genetic algorithms.

CRediT authorship contribution statement

Yaozhen Guo: Conceptualization, Investigation, Software, Writing - original draft. **Di Yuan:** Investigation. **Zhongrui Li:** Data curation, Formal analysis, Software. **Chenyu Zhu:** Data curation, Formal analysis, Software. **Zixuan Dai:** Data curation, Formal analysis, Software. **Bo Liu:** Funding acquisition, Methodology, Project administration, Supervision, Writing - review & editing.

Acknowledgments

This work is supported by the National Natural Science Foundation of China (Grant No. 11975168) and the Open Project of the State Key Laboratory of Intense Pulsed Radiation Simulation and Effect (Grant No. SKLIPR2022).

Declaration of competing interest

The authors declare that they have no known competing financial interests or personal relationships that could have appeared to influence the work reported in this paper.

Appendix A. Calculation details for the light intensity distribution of an individual microlens

As shown in Fig. 6(a), the vertical and horizontal distances between scintillation light source and microlens are defined as H and R, respectively. φ_1 denotes the half-apex angle of the escape cone. β = arctan (H/R) is the angle at the symmetry axis of the escape cone. i_1 and i_2 are the incident and emergence angles, respectively. We have the geometrical relationship with formula (3).

$$\frac{\sin(\beta+\varphi_2-i_1)}{r}=\frac{\sin(\beta)\sin(\beta+\varphi_1)}{\sin(\varphi_1)\sqrt{H^2+R^2}} \tag{3}$$

According to the law of refraction, we have i_2 = arcsin$[n_2\sin(i_1)]$. Thus, we can obtain the expression of light intensity of an individual microlens by formula (4).

$$I_0'=\frac{I_0}{2}\left[\frac{\sin(2i_1)\sin(2i_2)}{\sin^2(i_1+i_2)}+\frac{\sin(2i_1)\sin(2i_2)}{\sin^2(i_1+i_2)\cos^2(i_1-i_2)}\right] \tag{4}$$

The spatial distribution of this individual microlens is shown in Fig. 6(b). Where, the distribution is symmetric about angle β. And the maximum range of the distribution (γ_{max}) is calculated by formula (5).

$$\gamma_{max}=\arcsin\frac{1}{n_2}+\arcsin\frac{D/2}{n_1\sqrt{H^2+R^2}} \tag{5}$$

Therefore, the angle β determines the direction of the symmetry axis and the γ_{max} determines the size of escape cone. When $\beta < \gamma_{max,}$negative-angle distribution appears, which overlaps with other distribution.

Appendix B. Transformation of coordinates

A transformational equation is used to correct the relative position between the scintillation light source and the center of the individual microlens, which is related to the projection of the escape cone onto the plane. Fig. 7 shows the coordinate systems before and after transformation. An orthogonal transformation matrix is given by formula (6). Where, φ_3 is the inclination angle of an inclined ellipse. This is a standard method to transform a normal ellipse into an inclined ellipse [22].

$$\begin{bmatrix}x'\\y'\end{bmatrix}=\begin{bmatrix}\cos\varphi_3 & -\sin\varphi_3\\ \sin\varphi_3 & \cos\varphi_3\end{bmatrix}\begin{bmatrix}x\\y\end{bmatrix} \tag{6}$$

Thus, the transfer equation can be given by formula (7).

$$\begin{cases}x=r'\cos(\theta+\frac{\pi}{2})\cos(\varphi_3)-r'\cos(\varphi_1)\sin(\theta+\frac{\pi}{2})\sin(\varphi_3)\\ y=r'\cos(\theta+\frac{\pi}{2})\sin(\varphi_3)+r'\cos(\varphi_1)\sin(\theta+\frac{\pi}{2})\cos(\varphi_3)\\ z=h-\frac{r}{H}(x+y)\\ r'=r\sin(\varphi_2)\\ \theta\in(0,2\pi)\\ \varphi_2\in(0,\varphi_{2-max})\end{cases} \tag{7}$$

Appendix C. Genetic algorithms and operational logic

The genetic algorithms have six steps: encoding, swap, mutation, inversion, evaluation and copy. In the encoding step, the variables are encoded to binary series which have length of k. The binary form of variables also could be called as gene. The relationship between the binary form of $b_k b_{k-1}\ldots b_3 b_2 b_1$ and the origin value of x is as below.

$$x=L=(\sum_{i=1}^{k}b_i 2^{i-1})(\frac{U-L}{2^k-1}) \tag{8}$$

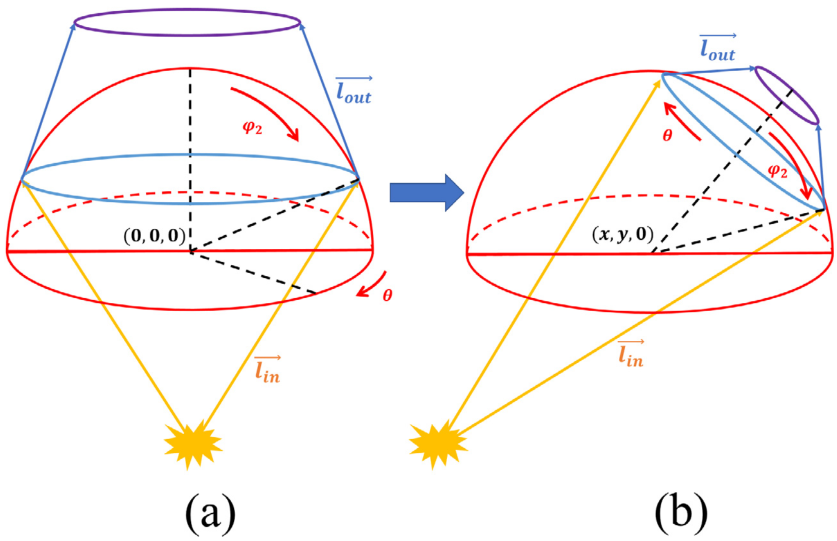

Fig. 7. (a) Coordinate system before transformation. (b) Coordinate system after transformation.

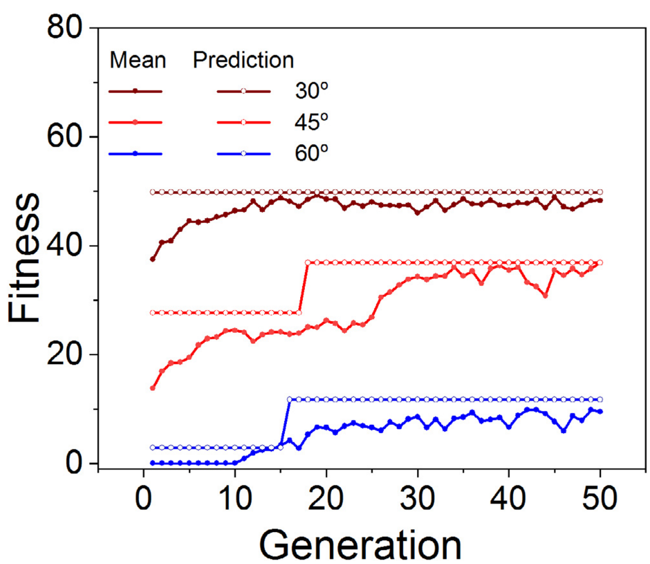

Fig. 8. Fitness-generation curve in the genetic algorithms.

Where U and L are the upper bound and the lower bound of the variables, respectively. The precision of variables can be expressed as formula (9).

$$\delta = \frac{U - L}{2^k - 1} \quad (9)$$

The swap process starts after the encoding process has finished. In this process, two genes are selected randomly from gene pools. The part of genes will be swap by generating a random swap point. In the mutation process, a gene is chosen randomly, followed by a change of value in a random point. In the inversion process, the order of a gene will be inversed from a randomly selected start point. Next, the genes will be decoded, then the values of a target function will be calculated. In order to minimize the target function, the evaluation number is defined as formula (10).

$$eval = small_{num} + f(x_1, x_2) \quad (10)$$

The probability of copying to next generation of a gene is:

$$P_i = \frac{eval_i}{\sum_j eval_j} \quad (11)$$

The accumulated probability of a gene is:

$$Q_j = \sum_j P_j \quad (12)$$

Finally, a series of random numbers in [0, 1] will be generated, a gene Q_i will be copied to the next generation if and only if:

$$Q_i < rand \leq Q_{i+1} \quad (13)$$

Where, *rand* is a random number from 0 to 1. Apparently, the less the target value is, the larger the probability of copy is. After a sufficient number of iterations, the group will converge finally. Fig. 8 displays the fitness curve for values of V, the fitness converges to the predicted curve and thus the calculated result is of great reference value.

References

[1] Q. Li, X. Liu, M. Gu, Y. Hu, F. Li, S. Liu, Q. Wu, Z. Sun, J. Zhang, S. Huang, Opt. Express 26 (2018) 31290–31298.
[2] H. Chen, M. Gu, Z. Sun, X. Liu, B. Liu, J. Zhang, S. Huang, C. Ni, Opt. Express 27 (2019) 14871–14880.
[3] A. Chilingarian, G. Hovsepyan, E. Mnatsakanyan, Phys. Rev. D 93 (2016) 052006.
[4] W. Heiss, C. Brabec, Nature Photonics 10 (2016) 288.
[5] C. Struebing, J. Chong, G. Lee, M. Zavala, A. Erickson, Y. Ding, C.-L. Wang, Y. Diawara, R. Engels, B. Wagner, Appl. Phys. Lett. 108 (2016) 153106.
[6] M. Nikl, A. Yoshikawa, Adv. Opt. Mater. 3 (2015) 463–481.
[7] X. Chen, B. Liu, Q. Wu, Z. Zhu, J. Zhu, M. Gu, H. Chen, J. Liu, L. Chen, X. Ouyang, Opt. Express 26 (2018) 11438–11446.
[8] J. Liu, B. Liu, Z. Zhu, L. Chen, J. Hu, M. Xu, C. Cheng, X. Ouyang, Z. Zhang, J. Ruan, Opt. Lett. 42 (2017) 987–990.
[9] M. Salomoni, R. Pots, P. Lecoq, E. Auffray, S. Gundacker, M. Paganoni, B. Singh, M. Marshall, V.V. Nagarkar, IEEE Trans. Nucl. Sci. 65 (2018) 2191–2195.
[10] M. Salomoni, R. Pots, E. Auffray, P. Lecoq, Crystals 8 (2018) 78.
[11] Z. Zhu, B. Liu, C. Cheng, H. Zhang, H. Chen, M. Gu, J. Liu, L. Chen, X. Ouyang, C. Xue, Appl. Phys. Lett. 110 (2017) 051901.
[12] B. Liu, Q. Wu, Z. Zhu, C. Cheng, M. Gu, J. Xu, H. Chen, J. Liu, L. Chen, Z. Zhang, Appl. Phys. Lett. 111 (2017) 081904.
[13] B. Liu, Z. Zhu, J. Zhu, S. Wu, H. Chen, M. Gu, Q. Cheng, H. Chen, C. Cheng, Z. Wang, Appl. Phys. Lett. 104 (2014) 061902.
[14] B. Liu, Z. Zhu, Q. Wu, C. Cheng, M. Gu, J. Xu, H. Chen, J. Liu, L. Chen, X. Ouyang, Appl. Phys. Lett. 110 (2017) 181905.
[15] S.-I. Chang, J.-B. Yoon, H. Kim, J.-J. Kim, B.-K. Lee, D.H. Shin, Opt. Lett. 31 (2006) 3016–3018.
[16] X.-H. Lee, I. Moreno, C.-C. Sun, Opt. Express 21 (2013) 10612–10621.
[17] Y.M. Song, Y. Xie, V. Malyarchuk, J. Xiao, I. Jung, K.-J. Choi, Z. Liu, H. Park, C. Lu, R.-H. Kim, Nature 497 (2013) 95–99.
[18] H.S. Kim, S.I. Moon, D.E. Hwang, K.W. Jeong, C.K. Kim, D.-G. Moon, C. Hong, Opt. Laser Technol. 77 (2016) 104–110.
[19] K. Binder, D.W. Heermann, Comput. Phys. 7 (1988) 156.
[20] U. Maulik, S. Bandyopadhyay, Pattern Recognit. 33 (2000) 1455–1465.
[21] V. Kreinovich, C. Quintana, O. Fuentes, Cybern. Syst. 24 (1993) 9–26.
[22] E. Kovács, Ann. Math. Inform. 40 (2012) 175–186.